



# A single-atom Fe-N-C catalyst with superior Fenton-like reaction performance prepared facilely using microalgae: Key roles of oxygen and interactions between Fe-N<sub>x</sub> and Fe/Fe compounds

Cheng Hou <sup>a,1</sup>, Jiang Zhao <sup>a,c,1</sup>, Libin Yang <sup>a</sup>, Jiabin Chen <sup>a</sup>, Xuefen Xia <sup>a</sup>, Xuefei Zhou <sup>a,b</sup>,  
Yalei Zhang <sup>a,b,\*</sup>

<sup>a</sup> State Key Laboratory of Pollution Control and Resources Reuse, College of Environmental Science and Engineering, Tongji University, Shanghai 200092, PR China

<sup>b</sup> Shanghai Institute of Pollution Control and Ecological Security, Shanghai 200092, PR China

<sup>c</sup> Shanghai Rural Revitalization Research Center, Shanghai 200002, PR China



## ARTICLE INFO

### Keywords:

Single-atom catalyst  
Fenton-like process  
Biochar  
Microalgae  
Fe-N-co-doped carbon-based catalyst

## ABSTRACT

A single-atom Fe-N-C catalysts (Fe-N-C) was successfully prepared through a facile synthesis route using microalgae to drive hydrogen peroxide (H<sub>2</sub>O<sub>2</sub>)-based Fenton-like reactions. The detailed characterization analyses confirmed the simultaneous presence of Fe/Fe compounds and Fe-N<sub>x</sub> coordination sites in the optimal catalyst (Fe-N @ MBC) obtained through the pyrolysis of FeCl<sub>3</sub>-6 H<sub>2</sub>O and *Chlorella vulgaris*. Surprisingly, when applied in H<sub>2</sub>O<sub>2</sub>-based advanced oxidation processes (AOPs), Fe-N @ MBC demonstrated excellent proficiency for both H<sub>2</sub>O<sub>2</sub> and O<sub>2</sub> activation, with the contribution of the original dissolved oxygen for sulfamethoxazole removal reaching up to 47.59%. The experiment and density functional theory (DFT) calculation results indicated that the Fe/Fe compounds significantly boosted the activity of Fe-N<sub>x</sub> by lowering the energy barrier of the reactive oxygen species formation and promoting the electron transfer between Fe-N<sub>x</sub> and the oxidants (H<sub>2</sub>O<sub>2</sub> and O<sub>2</sub>). These findings provide new insights into the facile synthesis, rational design, and catalytic mechanisms of Fe-N-C used in H<sub>2</sub>O<sub>2</sub>-based AOPs.

## 1. Introduction

As the population continues to burgeon and industrialization accelerates, numerous reports have forecasted that the demand for energy will reach between 800 and 900 EJ by 2040, signifying a substantial increase in the consumption of fossil fuels [1]. Nonetheless, the widespread utilization of fossil fuels will give rise to issues such as the greenhouse effect and water pollution, posing a threat to the sustainable development of humanity [2–4]. Hence, it is of significant importance to seek out a renewable and green energy source to address the energy crisis. Microalgae, a readily available and renewable biomass, has been widely used in biofuels production due to its advantages, such as high growth rate, high lipid content, and no need for arable land [5–7]. Out of numerous microalgae conversion technologies, pyrolysis is a widely researched method for transforming microalgae into bio-oil [8]. In the process of producing bio-oil through microalgae pyrolysis, a significant

amount of biochar (15–43%) is also produced [8]. Thus, exploring the efficient utilization of microalgae pyrolysis biochar is a topic worthy of investigation.

In recent years, evidence has shown that N-doped biochar is capable of effectively removing pollutants from water [9]. As a result, some studies have started to focus on N-containing compounds within microalgae cells as an inherent source of N doping in microalgae biochar [10,11]. As an example, a N-doped graphitic biochar was successfully synthesized from *Spirulina* residue after C-phycocyanin extraction. This biochar was found to have the ability to degrade sulfamethoxazole (SMX) through an advanced oxidation process (AOP) employing peroxydisulfate (PDS) [10]. In addition, single-atom Fe-N-C catalysts (Fe-N-C), which are carbon matrices co-doped with Fe and nitrogen, can be synthesized through the pyrolysis of hybrids consisting of carbon matrices, Fe-containing complexes, and nitrogen-containing precursors [12]. Therefore, pyrolysis of microalgae with the addition of Fe presents

\* Corresponding author at: State Key Laboratory of Pollution Control and Resources Reuse, College of Environmental Science and Engineering, Tongji University, Shanghai 200092, PR China.

E-mail address: [zhangyalei@tongji.edu.cn](mailto:zhangyalei@tongji.edu.cn) (Y. Zhang).

<sup>1</sup> These authors contributed equally to this work and should be considered co-first authors.

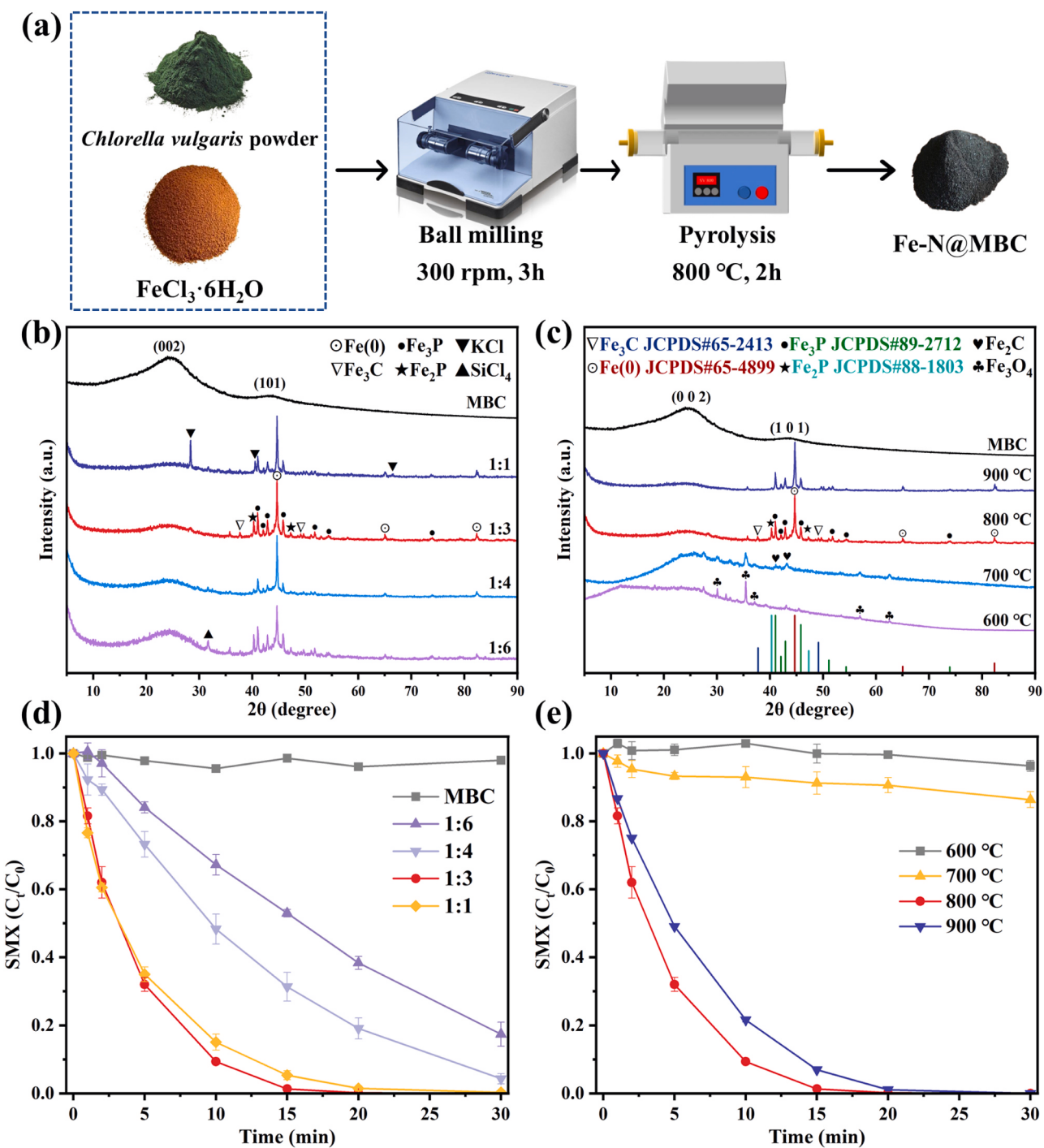


**Fig. 1.** (a) Synthesis scheme of Fe-N@MBC. (b, c) XRD patterns of different composites. (d, e) Activation performances of different composites. Reaction conditions: [catalyst] = 50 mg/L,  $[\text{H}_2\text{O}_2]$  = 0.3 mM, [SMX] = 20  $\mu\text{M}$ , and initial pH = 3.3.

a promising opportunity for the production of Fe-N-C. However, there is currently a dearth of research on the direct pyrolysis of hybrids consisting of microalgae and Fe for Fe-N-C synthesis.

Fe-N-C has recently emerged as a cutting-edge catalyst in AOPs, thanks to its exceptional atomic utilization efficiency and intrinsic activity [11,13]. Nonetheless, Fe-N-C may comprise multiple phases, including metal Fe (zero-valent iron, ZVI), Fe compounds (e.g.,  $\text{Fe}_x\text{C}$  and  $\text{FeO}_x$ ), and Fe-N<sub>x</sub> sites, posing a challenge to the comprehension of catalytic mechanisms based on Fe-N-C [11,14–16]. In the past few years, much effort has been exerted to gain insight into the high activity of Fe-N-C in electrochemical reactions [17–19]. Notably, one study pointed

out that the interactions between Fe/Fe<sub>3</sub>C and Fe-N<sub>x</sub> in Fe-N-C electrocatalysts could facilitate oxygen adsorption, subsequently enhancing the activity of Fe-N<sub>x</sub> in oxygen reduction reactions [15]. However, the use of Fe-N-C for AOPs has received significantly less attention compared to electrochemical reactions. Currently, only a few studies have probed the activation of PDS and peroxymonosulfate using Fe-N-C for the degradation of organic pollutants [11,20,21]. It is worth noting that while hydrogen peroxide ( $\text{H}_2\text{O}_2$ )-based AOPs are widely recognized as highly effective for degrading organic pollutants, there has been limited research on  $\text{H}_2\text{O}_2$ -based AOPs utilizing Fe-N-C to the best of our knowledge [22]. Thus, it is imperative to gain a deeper understanding of

the mechanisms involved in the removal of pollutants through  $\text{H}_2\text{O}_2$ -based AOPs utilizing Fe-N-C.

Herein, we developed a facile synthesis route of Fe-N-C using microalgae (Fig. 1a) and studied its performance and mechanisms in  $\text{H}_2\text{O}_2$ -based AOPs. Initially, the synthesis parameters were optimized based on the removal efficiency of SMX in the  $\text{H}_2\text{O}_2$  system. Subsequently, the microstructure and coordination environment of Fe atoms of the *Chlorella vulgaris*-derived Fe-N-C catalyst prepared under the optimal condition (Fe-N @ MBC) were characterized. Then, Fe-N @ MBC was further employed in the  $\text{H}_2\text{O}_2$  system for SMX degradation to explore the removal mechanisms. Moreover, desorption and  $\text{N}_2$ -sparging experiments were conducted to quantify the contribution of different ways to SMX removal. Additionally, the reactive species participating in the Fe-N @ MBC/ $\text{H}_2\text{O}_2$  process were determined by electron paramagnetic resonance (EPR) analysis. Interestingly, we found that the interactions between Fe-N<sub>x</sub> and Fe/Fe compounds played a crucial role in the exceptional activity of Fe-N @ MBC for activating  $\text{O}_2$  and  $\text{H}_2\text{O}_2$ . Then, the underlying mechanisms were unveiled by density functional theory (DFT) calculations.

## 2. Materials and methods

### 2.1. Materials

*Chlorella vulgaris*, a common microalgal strain, was used in this study. The *Chlorella vulgaris* powder ( $\geq 98\%$ ) was obtained from Xi'an Wusehua Biotechnology Co., Ltd (Xi'an, China). SMX was supplied by Sigma-Aldrich (St. Louis, MO).  $\text{H}_2\text{O}_2$  (30% w/w) and iron chloride hexahydrate ( $\text{FeCl}_3 \cdot 6 \text{ H}_2\text{O}$ ) were purchased from Aladdin (Shanghai, China). The detailed information of other chemical reagents sources is shown in Text S1.

### 2.2. Synthesis of Fe-N @ MBC

As illustrated in Fig. 1a, Fe-N @ MBC was prepared by a facile two-step route. Typically, 0.5 g  $\text{FeCl}_3 \cdot 6 \text{ H}_2\text{O}$  and 1.5 g *Chlorella vulgaris* powder (mass ratio of 1:3) were ball milled for 3 h at 300 rpm. Then, the mixture was pyrolyzed at 800 °C for 2 h with a heating rate of 5 °C/min in a horizontal tube furnace under  $\text{N}_2$  flow. Finally, the product was ground into powder and labeled as Fe-N @ MBC. For comparison, pristine microalgae biochar (MBC) was synthesized using the same method without adding  $\text{FeCl}_3 \cdot 6 \text{ H}_2\text{O}$ . When studying the effects of mass ratio (1:1, 1:3, 1:4, and 1:6), the samples were all pyrolyzed at 800 °C, while for the investigation of the effects of pyrolysis temperature (600, 700, 800, and 900 °C), the mass ratio of  $\text{FeCl}_3 \cdot 6 \text{ H}_2\text{O}$  to *Chlorella vulgaris* powder was kept fixed at 1:3. The characterization methods for the composites were detailed in Text S2.

### 2.3. Degradation experiments

The degradation experiments were all performed in a shaking table concentrator (180 rpm and 25 °C). Typically, 0.3 mM  $\text{H}_2\text{O}_2$ , 20  $\mu\text{M}$  SMX and deionized water were mixed in a 250 mL Erlenmeyer flask reaching a total volume of 100 mL, and the solution pH was adjusted to 3.3 using 0.5 M HCl and 0.5 M NaOH (if necessary) immediately. After that, the catalytic reaction was triggered by dosing 5.0 mg Fe-N @ MBC (50 mg/L). At predetermined time intervals, samples were extracted and quenched with excess methanol before detecting SMX concentration. The samples were stored at 4 °C prior to analysis. To quantify the removal rate of SMX by adsorption, the desorption experiment was conducted. Specifically, Fe-N @ MBC separated from the solution after the degradation experiment was extracted with a 100 mL mixture of acetic acid and methanol (volume ratio = 1:9) for 30 min, and then the suspension was filtered through a filter (0.22  $\mu\text{m}$ ) for analysis [23]. All the experiments were conducted in duplicates or more.

### 2.4. Analytic methods

The concentrations of SMX and other selected pollutants were detected by high-performance liquid chromatography (HPLC) (see Table S1 for details). The transformation products of SMX were measured by an ultraperformance liquid chromatography (UPLC, Agilent 1290 Infinity, USA)-tandem mass spectrometry (MS/MS, Agilent 6550 QTOF, USA), and the details are provided in Text S3. The acute and chronic toxicity of SMX and its transformation products were estimated by Ecological Structure-Activity Relationship Model (ECOSAR) program (Text S3) [24]. EPR spectrometer was used to determine the reactive oxygen species (ROS) in the Fe-N @ MBC/ $\text{H}_2\text{O}_2$ , Fe-N @ MBC, and Fe-N @ MBC/ $\text{N}_2$  systems (Text S3). All the calculations based on DFT were performed using the Vienna Ab Initio Simulation Package (VASP), as detailed in Text S3.

## 3. Results and discussion

### 3.1. Preparation and basic properties of Fe-N @ MBC

#### 3.1.1. Structure and phase composition analyses

The X-ray diffraction (XRD) patterns and detailed information confirming the structure and phase composition of the composites prepared under different conditions are presented in Fig. 1b-c and Table S2, respectively. MBC exhibited two broad diffraction peaks in the ranges of 20–30° and 40–45°, corresponding to the (0 0 2) and (1 0 1) reflections of graphitized carbon (Fig. 1b-c) [25]. Upon the addition of  $\text{FeCl}_3 \cdot 6 \text{ H}_2\text{O}$ , peaks associated with iron were detected, including crystalline phases of metallic iron (Fe (iron, JCPDS#65–4899)) and iron compounds ( $\text{Fe}_3\text{C}$  (iron carbide, JCPDS#65–2413),  $\text{Fe}_3\text{P}$  (iron phosphide, JCPDS#89–2712), and  $\text{Fe}_2\text{P}$  (barringerite, JCPDS#88–1803)) in 1:6, 1:4, and 1:3. Notably, the characteristic peaks of  $\text{Fe}_2\text{P}$  in 1:1 disappeared, and the diffraction peaks of  $\text{KCl}$  and  $\text{SiCl}_4$  appeared in 1:1 and 1:6, respectively, indicating that the addition content of  $\text{FeCl}_3 \cdot 6 \text{ H}_2\text{O}$  influenced the phase composition of the composites. Furthermore, the effects of pyrolysis temperature on the phase composition were studied (Fig. 1c). The composites prepared at 600 °C and 700 °C mainly consisted of  $\text{Fe}_3\text{O}_4$ , while at 800 °C,  $\text{Fe}_3\text{O}_4$  was transformed to Fe (0),  $\text{Fe}_3\text{C}$ ,  $\text{Fe}_3\text{P}$ , and  $\text{Fe}_2\text{P}$ . For clarity, the standard cards of Fe and Fe compounds are provided in Fig. 1c. Notably, no diffraction peaks of  $\text{Fe}_3\text{C}$  and  $\text{Fe}_2\text{P}$  appeared in 900 °C. Based on these XRD results and previous literature, the formation of Fe/Fe compounds was derived from the reduction of the iron precursor by carbon and reducing gases during pyrolysis [15,26, 27].

#### 3.1.2. Surface characteristic analyses

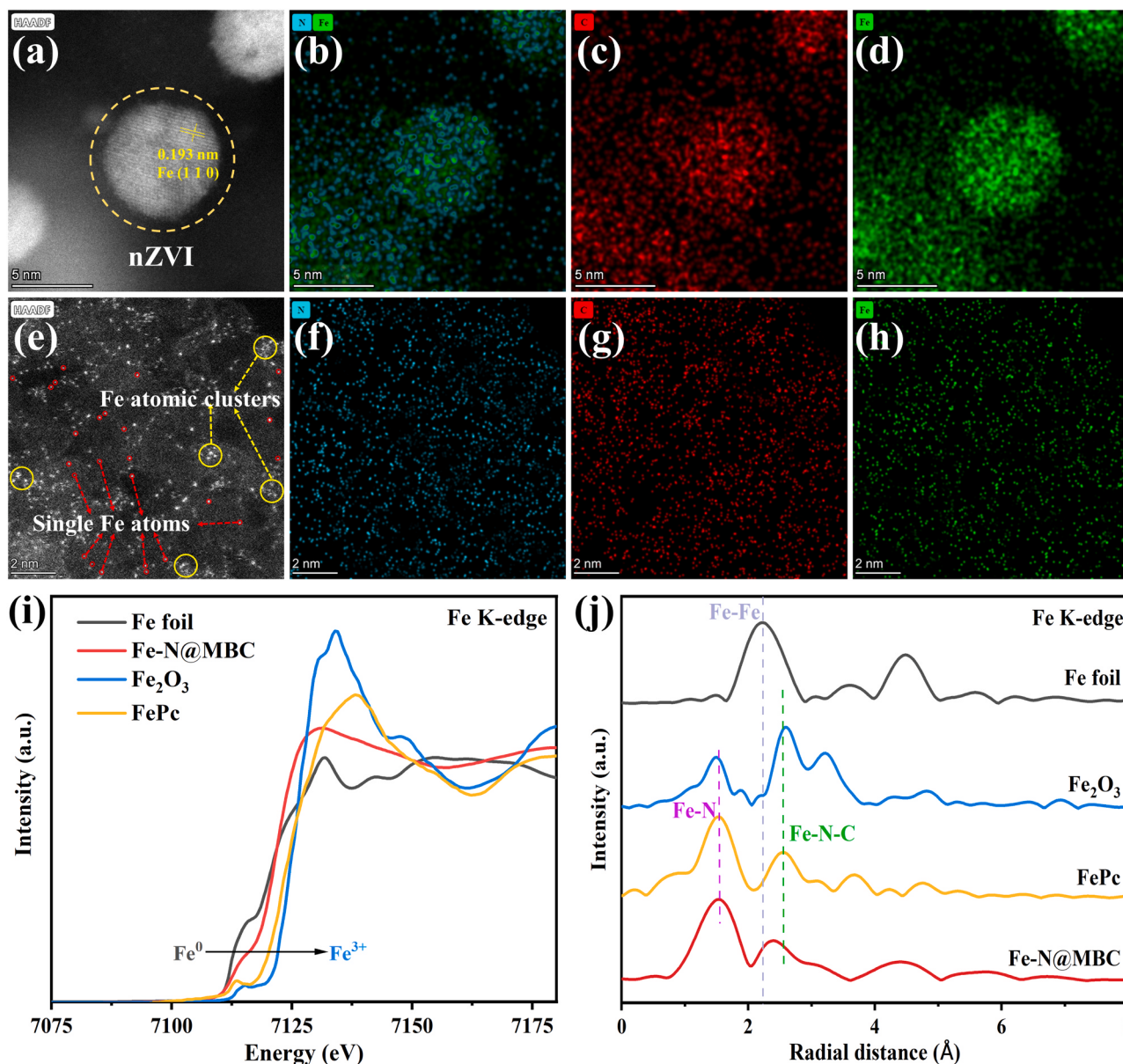
The composites were subjected to X-ray photoelectron spectroscopy (XPS) to investigate their surface characteristics (Figs. S1–S4 and Table S3). The high-resolution XPS spectra of Fe 2p3/2 were analyzed and fitted to Fe-N (710.75 eV) and Fe-O (712.25 eV) (Fig. S1), but no peak of Fe (0) was detected [28,29]. It is known that only surface or subsurface species can be detected by XPS [30]. In this study, the Fe (0) particles were enveloped by thick carbon layers in these composites, which will be discussed in Section 3.2. Therefore, the absence of Fe (0) in Fe 2p3/2 spectra is reasonable. Fig. S2 shows that the N 1 s spectra were curve-fitted with five peaks at most with binding energies of 398.25, 399.56, 400.60, 401.10, and 402.20 eV, attributed to pyridinic N, Fe-N, pyrrolic N, graphitic N and oxidized N, respectively [25]. The high-resolution XPS spectra of O 1 s could be deconvoluted into three peaks at most with binding energies of 530.27, 531.63, and 532.71 eV, which were assigned to C-O-C/C-OH, O-C=O/C=O, and Fe-O, respectively (Fig. S3) [31]. As for the XPS C 1 s, five peaks with the binding energies at 284.40, 284.90, 285.50, 286.60, and 289.08 eV were assigned to C=C, C-C, C-O, C=O, and O-C=O, respectively (Fig. S4) [31,32]. These results indicated that the synthesis conditions affected the surface characteristics of the composites, especially the N and O

**Table 1**

Main elements and BET surface areas of the composites synthesized under different conditions.

Samples	Ash <sup>a</sup>	C <sup>a</sup>	H <sup>a</sup>	N <sup>a</sup>	S <sup>a</sup>	O <sup>a</sup>	S <sub>BET</sub> (m <sup>2</sup> /g)	Fe (g/kg)
M	2.83	43.13	6.02	4.59	0.62	42.81	NT	0.10
MBC	11.46	69.69	1.49	3.33	0.28	13.76	456.28	7.72
1:1	51.89	43.05	1.17	2.14	0.80	0.96	598.47	347.80
1:3 <sup>b</sup>	33.58	59.32	1.42	3.30	0.66	1.72	624.88	199.00
1:4	26.43	58.04	1.17	2.30	0.59	11.48	652.29	151.30
1:6	21.84	63.56	1.34	2.99	0.52	9.76	468.78	87.98
600	26.75	49.33	1.55	3.89	0.40	18.09	5.42	112.50
700	30.38	48.93	1.56	3.38	0.49	15.26	276.54	162.30
800 <sup>b</sup>	33.58	59.32	1.42	3.30	0.66	1.72	624.88	199.00
900	33.63	62.82	0.61	1.71	0.75	0.48	553.73	165.81

NT: Not tested.

<sup>a</sup> Mass ratio.<sup>b</sup> 1:3 and 800 °C represent the same composite (i.e., Fe-N @ MBC).

**Fig. 2.** (a) 5 nm HAADF-STEM image of Fe-N @ MBC and (b-d) corresponding EDS mapping images. (e) 2 nm HAADF-STEM image of Fe-N @ MBC and (f-h) corresponding EDS mapping images. (i) Fe K-edge XANES spectra and (j) Fourier transformed EXAFS spectra of Fe-N @ MBC, Fe foil, Fe<sub>2</sub>O<sub>3</sub>, and iron phthalocyanine (FePc).

characteristics (Table S3).

### 3.1.3. Elemental composition and specific surface area analyses

The main elements and BET surface areas ( $S_{BET}$ ) of the composites are listed in Table 1. The high N content of microalgae (M) and the composites derived from microalgae indicated that the abundant nitrogen-containing compounds in microalgae, such as polysaccharides and proteins, could be used as inherent N sources for N doping [10]. Generally, the contents of H, N, and O decreased with the increase in pyrolysis temperature, whereas the ash, C, and S contents increased. This is because the H, N, and O were consumed to produce volatile gases, resulting in the increase of ash, fixed C, and S during the pyrolysis process [33]. Moreover, the Fe content and  $S_{BET}$  increased initially and then decreased. With the temperature increased from 600 °C to 800 °C, the tar compounds in microalgae volatilized, increasing the Fe content and  $S_{BET}$ . When the temperature reached 900 °C, the reduction in Fe content could be attributed to the decrease of N and O contents, which can interact with Fe to form compounds. In addition, the diminution of nanoscale Fe species featuring high surface area and the blocked effect arising from ash melting resulted in the decrease of the  $S_{BET}$  [34,35]. Regarding the effects of the mass ratio of  $\text{FeCl}_3 \cdot 6 \text{H}_2\text{O}$  to *Chlorella vulgaris* powder, the ash and Fe contents increased with the increase of mass ratio, whereas C and O contents decreased. Moreover, the mass ratio had little effect on the H, N, and S contents of the composites. The  $S_{BET}$  of MBC, 1:6, and 1:4 was 456.28, 468.78, and 652.29  $\text{m}^2/\text{g}$ , respectively, indicating the addition of Fe was beneficial to the  $S_{BET}$ . However, when the addition amount further increased to 1:3 and 1:1, the excessive Fe aggregated and blocked the pores, resulting in the  $S_{BET}$  decrease of 1:3 (624.88  $\text{m}^2/\text{g}$ ) and 1:1 (598.47  $\text{m}^2/\text{g}$ ) [36].

### 3.1.4. Removal performance of different composites

Fig. 1d and e illustrate the removal efficiencies of SMX by the composites prepared under different conditions. Regarding the composites prepared using different mass ratios, the removal efficiencies were determined to be 1.98%, 82.58%, 95.65%, 100%, and 99.69% for MBC, 1:6, 1:4, 1:3, and 1:1, respectively (Fig. 1d). These results suggest that the introduction of iron species played a crucial role in SMX removal. In addition, the SMX removal rate was significantly higher for 1:6 (82.58%) compared to MBC (1.98%), while the  $S_{BET}$  of 1:6 (468.78  $\text{m}^2/\text{g}$ ) was slightly higher than that of MBC (456.28  $\text{m}^2/\text{g}$ ). Furthermore, despite the larger  $S_{BET}$  of 1:4 (652.29  $\text{m}^2/\text{g}$ ) compared to 1:3 (624.88  $\text{m}^2/\text{g}$ ) and 1:1 (598.47  $\text{m}^2/\text{g}$ ), 1:4 exhibited a lower removal rate for SMX, indicating that the adsorption played a negligible role in the removal of SMX. Fig. 1e shows that 3.64%, 13.62%, and 100% of SMX were removed by 600 °C, 700 °C, and 800 °C, respectively. Although the SMX removal efficiency of 900 °C was also 100%, the reaction rate was lower than that of 800 °C. Taking the XRD results into consideration, it can be inferred that the high activation performance was mainly attributed to the presence of Fe/Fe compounds ( $\text{Fe}_3\text{C}$ ,  $\text{Fe}_3\text{P}$ , and  $\text{Fe}_2\text{P}$ ). According to the removal efficiency of SMX, the optimal synthesis conditions for further study were chosen as 1:3 and 800 °C (i.e., Fe-N @ MBC).

## 3.2. Atomic local structure of Fe-N @ MBC

### 3.2.1. Microstructure

The Fe-N @ MBC microstructure was analyzed using scanning electron microscopy (SEM) and transmission electron microscopy (TEM) (Fig. S5). Fig. S5a shows that Fe-N @ MBC had a diverse pore structure along with spherical particles on its surface. Additionally, Fe-N @ MBC contained nanoparticles of different diameters, with some encapsulated in carbon layers, as indicated by darker contrast (Fig. S5b). High angle annular dark field scanning TEM (HAADF-STEM) was employed to examine the distribution of Fe atoms in Fe-N @ MBC. The HAADF-STEM image of Fe-N @ MBC in Fig. 2a reveals that the spherical particle has a lattice spacing of 0.193 nm, corresponding to the (1 1 0) plane of iron

(JCPDS#65–4899). This result is consistent with the XRD result, thereby proving that the spherical particles were nano zero-valent iron (nZVI) particles. Energy dispersive X-ray spectroscopy (EDS) mapping in Fig. 2b suggests that some nZVI particles were enveloped by carbon layers and surrounded by Fe and N atoms, aligning with the findings from the TEM analysis. This finding implies that the single-atom Fe was intimately associated with the nZVI particles in Fe-N @ MBC, promoting interactions between them. As shown in Fig. 2e, many scattered bright spots at atomic scale and clusters are distributed in Fe-N @ MBC, indicating that isolated Fe atoms and Fe clusters (Fe compounds) co-existed in Fe-N @ MBC. Moreover, corresponding EDS mapping images show that N and Fe were distributed uniformly in Fe-N @ MBC, suggesting Fe might be coordinated with inherent N of microalgae.

### 3.2.2. Coordination environment of Fe atoms

In an attempt to further clarify the coordination environment of the Fe atoms, X-ray absorption near-edge structure (XANES) and extended X-ray absorption fine structure (EXAFS) measurements were conducted. The results showed that the valence state of Fe atoms in Fe-N @ MBC was between  $\text{Fe}^{3+}$  and metallic Fe, as indicated by its near-edge absorption energy being situated between Fe foil and  $\text{Fe}_2\text{O}_3$  (Fig. 2i) [13]. The Fourier transformed EXAFS spectra of Fe-N @ MBC demonstrated a first shell peak at  $\sim 1.5 \text{ \AA}$ , which was attributed to the Fe-N scattering paths similar to iron phthalocyanine (FePc) (Fig. 2j). Moreover, the second shell peak at  $\sim 2.4 \text{ \AA}$  shifted to the right compared to the Fe-Fe scattering paths of Fe foil, which suggested Fe-N-C scattering paths. This indicates that the Fe species in Fe-N @ MBC were mainly isolated Fe atoms. Additionally, the wavelet transform (WT) plot of Fe-N @ MBC displayed a similar image to that of FePc (Fig. S6). Then, the quantitative structure information of the Fe atoms in Fe-N @ MBC was obtained by fitting EXAFS data (Fig. S7 and Table S4). The coordination numbers of Fe-N and Fe-N-C was 3.7 and 4.5 with a bond length of 2.036  $\text{\AA}$  and 2.900  $\text{\AA}$ , respectively, indicating the formation of  $\text{FeN}_4$  structure. The aforementioned results demonstrated that the synthesis of Fe-N-C via this approach utilizing microalgae was feasible.

## 3.3. Removal performance of the Fe-N @ MBC/ $\text{H}_2\text{O}_2$ system

### 3.3.1. Activation performance of Fe-N @ MBC

The activation performance of Fe-N @ MBC was evaluated by  $\text{H}_2\text{O}_2$  addition to remove SMX. As shown in Fig. S8a and Fig. S9, while 4.52% of  $\text{H}_2\text{O}_2$  was decomposed in 30 min, the removal rate of SMX by  $\text{H}_2\text{O}_2$  alone was close to zero, suggesting that SMX was unsusceptible to direct reaction with  $\text{H}_2\text{O}_2$ . Previous studies proposed that the persistent free radicals (PFRs) and transition metals in biochars could directly degrade organic pollutants and activate dissolved oxygen (DO) and  $\text{H}_2\text{O}_2$ , thereby generating reactive oxygen species (ROS) for organic pollutants destruction [37–39]. In this study, the negligible adsorption, direct degradation, and activation performance of MBC were proven by the fact that after 30 min, only 1.98% of SMX was removed by MBC alone (Fig. S8a). However, in the Fe-N @ MBC alone system, 50.88% of SMX was removed within the same duration. Additionally, SMX was utterly removed within 30 min in the Fe-N @ MBC/ $\text{H}_2\text{O}_2$  system, while merely 6.52% of SMX was removed in the MBC/ $\text{H}_2\text{O}_2$  system. Moreover, 65.93% of  $\text{H}_2\text{O}_2$  was decomposed in 30 min in the Fe-N @ MBC/ $\text{H}_2\text{O}_2$  system (Fig. S9). These results not only indicated that the inherent Fe (7.72 g/kg) and PFRs of MBC possessed ineffective activation performance towards  $\text{H}_2\text{O}_2$  and O<sub>2</sub> but also suggested that the iron addition played a crucial role in the high activation performance of Fe-N @ MBC.

To further identify the activation performance of Fe-N @ MBC, a modified kinetic constant ( $m \cdot k_{\text{obs}}$ ) was utilized [40]. The results showed that the  $m \cdot k_{\text{obs}}$  of the Fe-N @ MBC/ $\text{H}_2\text{O}_2$  system reached  $124 \text{ \mu mol} \cdot \text{min}^{-1} \cdot \text{g}^{-1}$ , which was significantly higher than those reported for other  $\text{H}_2\text{O}_2$ -based AOPs such as CoFe50 @C/ $\text{H}_2\text{O}_2$  and Fe/N-C MNCs/ $\text{H}_2\text{O}_2$  (Table S5). In summary, the enhancement was between 1.3 and 282.0-fold higher than those systems. This result demonstrated that

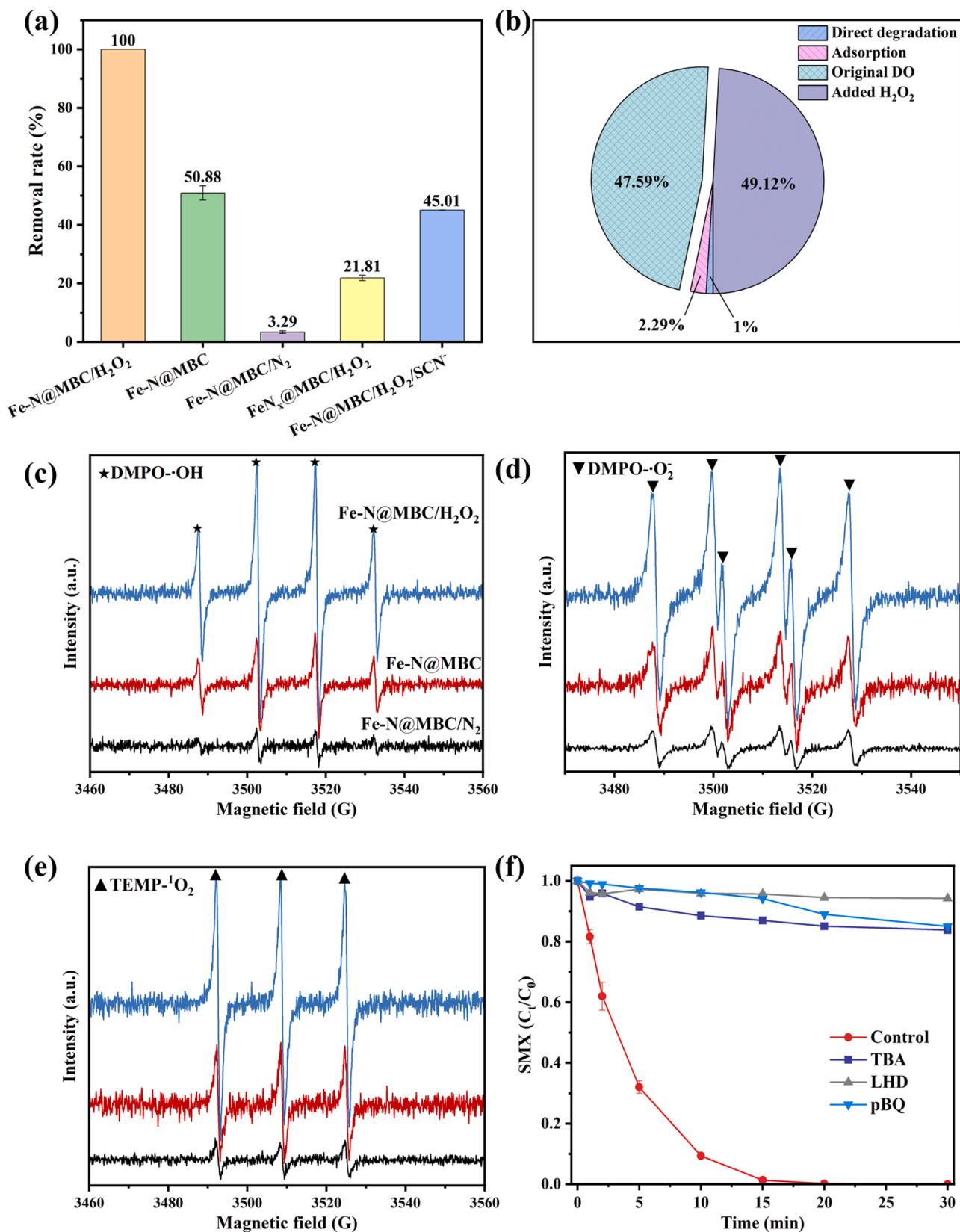


**Fig. 3.** (a) Removal rates of SMX in different systems. Reaction conditions: [catalyst] = 50 mg/L, [H<sub>2</sub>O<sub>2</sub>] = 0.3 mM, [SMX] = 20  $\mu$ M, [SCN<sup>-</sup>] = 10 mM, and initial pH = 3.3. (b) Contribution of different ways to SMX removal. Of these, the contribution of the original DO in the solution consisted of both O<sub>2</sub> and H<sub>2</sub>O<sub>2</sub> generated from O<sub>2</sub>. Additionally, the contribution of the added H<sub>2</sub>O<sub>2</sub> encompassed not only H<sub>2</sub>O<sub>2</sub>, but also O<sub>2</sub> resulting from the decomposition of H<sub>2</sub>O<sub>2</sub>. EPR spectra at 5 min obtained by spin trapping with (c) DMPO, (d) DMPO in methanol, and (e) TEMP in different systems. Reaction conditions: [catalyst] = 500 mg/L, [H<sub>2</sub>O<sub>2</sub>] = 3 mM, [DMPO] = [TEMP] = 100 mM, and initial pH = 3.3. (f) Effect of scavengers on SMX removal. Reaction conditions: [catalyst] = 50 mg/L, [H<sub>2</sub>O<sub>2</sub>] = 0.3 mM, [SMX] = 20  $\mu$ M, and initial pH = 3.3, if applied [TBA] = 205 mM, [LHD] = 10 mM, [BQ] = 0.3 mM.

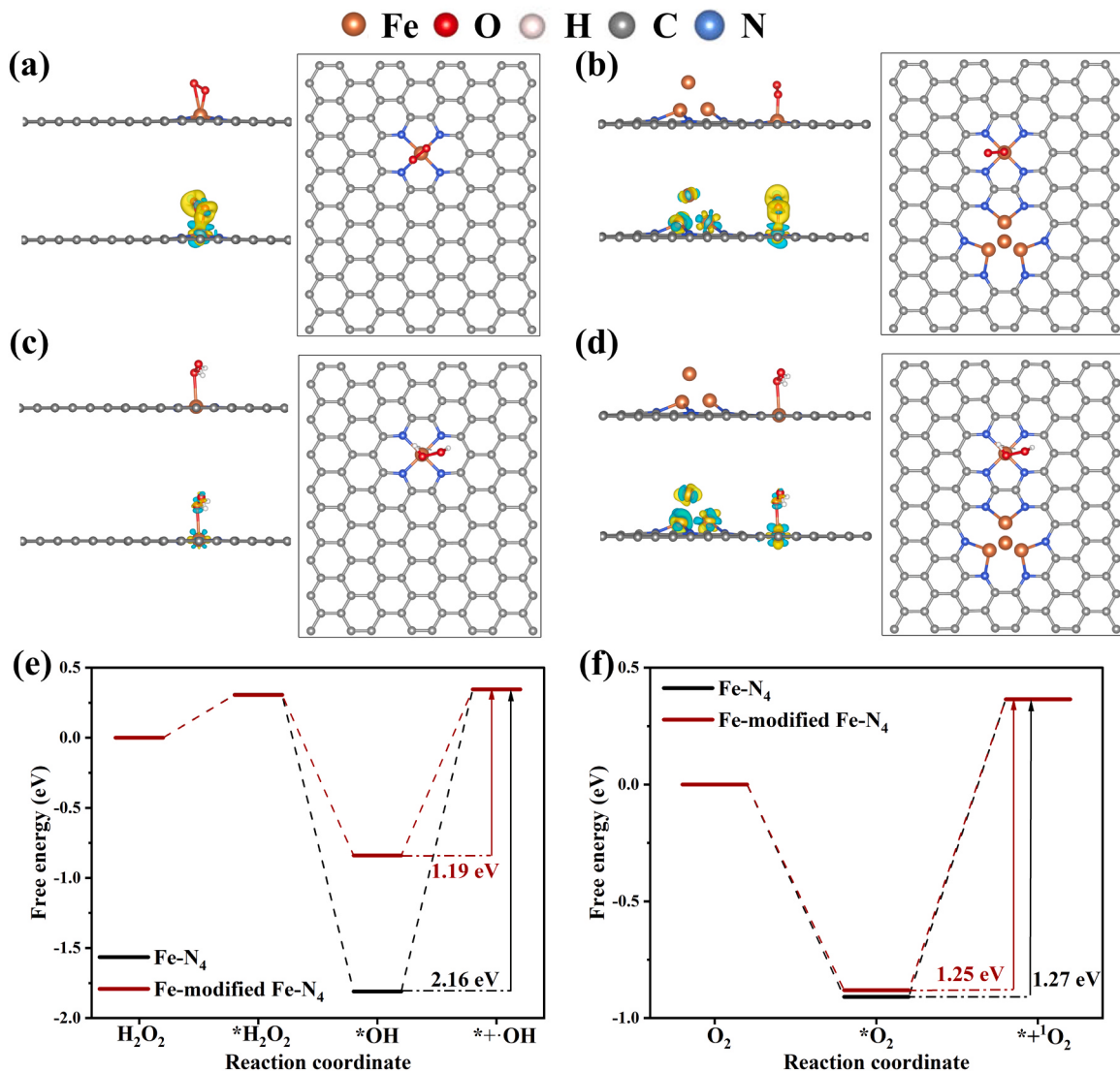


**Fig. 4.** Optimized adsorption structures of O<sub>2</sub> on (a) bare and (b) Fe-modified Fe-N<sub>4</sub> sites and corresponding charge density difference. Optimized adsorption structures of H<sub>2</sub>O<sub>2</sub> on (c) bare and (d) Fe-modified Fe-N<sub>4</sub> sites and corresponding charge density difference. Yellow bubbles represent electron accumulation, and cyan bubbles denote electron depletion. Free energy diagrams of the formation of (e)-OH and (f) <sup>1</sup>O<sub>2</sub>.

Fe-N @ MBC was an exceptional activator in H<sub>2</sub>O<sub>2</sub>-based systems. Furthermore, the universality of the Fe-N @ MBC/H<sub>2</sub>O<sub>2</sub> system was confirmed as it was effective in the complete degradation of various organic pollutants including sulfadiazine (SDZ), carbamazepine (CBZ), naproxen (NAP), phenol, and ciprofloxacin (CIP) within 30 min (Fig. S8f). The removal rates varied for each pollutant but were all successful. These results further indicated the effectiveness and versatility of the Fe-N @ MBC/H<sub>2</sub>O<sub>2</sub> system.

### 3.3.2. Effects of H<sub>2</sub>O<sub>2</sub> dosage, initial pH, and water matrices

The removal performance of the Fe-N @ MBC/H<sub>2</sub>O<sub>2</sub> system was also verified by investigating the effects of H<sub>2</sub>O<sub>2</sub> dosage, initial pH, and water matrices on SMX removal, as detailed in Text S4. With the H<sub>2</sub>O<sub>2</sub> dosage increased from 50  $\mu$ M to 300  $\mu$ M, the removal rate and fitted pseudo-first-order rate constants ( $k_{obs}$ ) increased from 88.5% to 100% and from 0.0748 min<sup>-1</sup> to 0.3102 min<sup>-1</sup> in 30 min, respectively. When the initial pH decreased from 8.70 to 3.30, the removal efficiency increased from 6.60% to 100%. However, when the solution pH further decreased from 3.30 to 2.28, the removal rate reduced from 100% to 72.19%. NO<sub>3</sub><sup>-</sup> and SO<sub>4</sub><sup>2-</sup> almost did not affect the removal of SMX in the Fe-N @ MBC/H<sub>2</sub>O<sub>2</sub> system, even though their concentration was as high as 100 mM.

As for Cl<sup>-</sup>, negligible inhibition of SMX destruction was observed as Cl<sup>-</sup> concentration ranging from 1 to 10 mM. Nevertheless, the removal rate of SMX dropped by 35.96% in 30 min when the Cl<sup>-</sup> concentration increased to 100 mM. With the increase in natural organic matter (humic acid, HA) addition, the SMX removal rates decreased, and the removal dropped by 5.09% at the HA concentration of 50 mg/L.

### 3.4. Removal mechanisms of SMX in the Fe-N @ MBC/H<sub>2</sub>O<sub>2</sub> system

#### 3.4.1. Contribution of different ways to SMX removal

According to previous literature, there are four main ways for organic pollutants removal in the biochar-based composites/H<sub>2</sub>O<sub>2</sub> processes: (i) adsorption due to the high SBET, good pore structures, and rich surface function groups; (ii) PFRs and transition metals on the surface of biochar-based composites directly degrade the organic pollutants; PFRs and transition metals activate (iii) H<sub>2</sub>O<sub>2</sub> and (iv) O<sub>2</sub> to produce ROS for organic pollutants destruction [28,41,42]. Thus, the SMX removal should be a complicated process in the Fe-N @ MBC/H<sub>2</sub>O<sub>2</sub> system.

To quantify the contribution of different ways for removing SMX, control experiments were conducted. As previously discussed, the Fe-N @ MBC alone system achieved a removal rate of 50.88%, which owed

to the adsorption, direct degradation, and the original DO in the solution, comprising of  $O_2$  and  $H_2O_2$  derived from  $O_2$  (as illustrated in Eq. (1)). Accordingly, the contribution of the added  $H_2O_2$ , including both the  $H_2O_2$  and  $O_2$  resulted from  $H_2O_2$  decomposition (Eq. (2)), accounted for 49.12%. Then, the  $N_2$ -sparging experiment was conducted in the Fe-N @ MBC alone system to investigate the contribution of the original DO in the solution. As shown in Fig. 3a, SMX removal decreased by 47.59% compared with the Fe-N @ MBC alone system after DO was eliminated by  $N_2$  sparging, demonstrating the significant contribution of original DO to SMX removal (47.59%). Moreover, the desorption result showed that 2.29% of SMX was removed via adsorption. Combining the results obtained from the Fe-N @ MBC/ $N_2$  system, the direct degradation of SMX by Fe-N @ MBC was calculated to be 1.00%. For clarity, the contribution of the four ways to SMX removal in the Fe-N @ MBC/ $H_2O_2$  system is illustrated in Fig. 3b.

#### 3.4.2. Identification of the ROS in the Fe-N @ MBC/ $H_2O_2$ system

Due to the low contribution of adsorption and direct degradation, the ROS derived from the activation of  $O_2$  and  $H_2O_2$  by Fe-N @ MBC played a vital role in SMX removal in the Fe-N @ MBC/ $H_2O_2$  system. Consequently, EPR analysis was performed in different systems to identify the ROS (Text S3). As shown in Fig. 3c-e, typical quadruplet DMPO-·OH, sextuplet DMPO- $O_2$ - and triplet TEMP- $^1O_2$  characteristic peaks at different intensities were detected in different systems, revealing the generation of ·OH,  $O_2\cdot$  and  $^1O_2$  [43,44]. More specifically, the intensity of these characteristic peaks increased after the addition of  $H_2O_2$ , whereas the intensity significantly decreased after eliminating  $O_2$  by  $N_2$  sparging. These results demonstrated that Fe-N @ MBC could activate  $H_2O_2$  and  $O_2$  to produce ROS. The weak peak intensity in the Fe-N @ MBC/ $N_2$  system might be due to the residual DO (0.61 mg/L) that could not be removed by  $N_2$  sparging, which showed the high activity of Fe-N @ MBC for  $O_2$  activation. Furthermore, the characteristic peak intensity increased during the reaction, while no peaks were observed without Fe-N @ MBC (0 min lines in Fig. S12), indicating that Fe-N @ MBC was essential for ROS generation. To substantiate the involvement of the ROS in SMX degradation, tert-butanol (TBA), L-histidine (LHD), and p-benzoquinone (pBQ) were employed as quenchers for ·OH,  $^1O_2$ , and  $O_2\cdot$ , respectively [27,28,45,46]. In the presence of TBA, LHD, and pBQ, the removal rate of SMX decreased to 16.23%, 5.77%, and 15.01% in 30 min, respectively (Fig. 3f). These results indicated that ·OH,  $O_2\cdot$  and  $^1O_2$  all played a role in the degradation of SMX.

#### 3.4.3. Insight into the significance of the interactions between Fe-N<sub>x</sub> and Fe/Fe compounds

As previously discussed, the Fe/Fe compounds might be necessary for the superior performance of Fe-N @ MBC. Therefore, a series of control experiments was conducted to further unveil the role of Fe/Fe compounds in  $H_2O_2$  and  $O_2$  activation by Fe-N @ MBC. At first, the Fe/Fe compounds in Fe-N @ MBC were removed or substantially diminished by acid, denoted as FeN<sub>x</sub> @MBC (see details in Fig. S13). The TEM images of FeN<sub>x</sub> @MBC show that the nanoparticles disappeared after acid-etching (Fig. S13). In addition, the ICP-MS results showed that only 2.90% of Fe remained in FeN<sub>x</sub> @MBC. The degradation experiment using FeN<sub>x</sub> @MBC showed a remarkable decrease in SMX removal, indicating that the Fe/Fe compounds were important for the high activation performance (Fig. 3a). Then, the degradation experiment was carried out using Fe-N @ MBC with the addition of SCN<sup>-</sup> to poison the Fe-N<sub>x</sub> sites [14,15]. As shown in Fig. 3a, the removal of SMX decreased to 45.01% in the presence of SCN<sup>-</sup>, implying the Fe-N<sub>x</sub> sites were responsible for the activation activity of Fe-N @ MBC. Moreover, the removal summation of these two experiments was less than that of the Fe-N @ MBC/ $H_2O_2$  system (100%). The results of these control experiments strongly supported the conclusion that the interactions between Fe-N<sub>x</sub> and Fe/Fe compounds were significant for the high activation performance of Fe-N @ MBC.

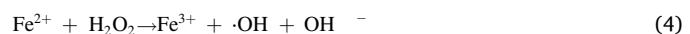
Subsequently, the DFT calculations were performed to elucidate the

interactions between Fe-N<sub>x</sub> and Fe/Fe compounds. Adsorption models were constructed for  $O_2$  and  $H_2O_2$  on both bare and Fe-modified Fe-N<sub>4</sub> moieties (Fig. 4). The adsorption energy ( $E_{ads}$ ) of  $O_2$  and  $H_2O_2$  on the bare Fe-N<sub>4</sub> sites was determined to be  $-0.836$  eV and  $-0.385$  eV, respectively. Upon introduction of the Fe cluster, the  $E_{ads}$  of  $O_2$  and  $H_2O_2$  on the Fe-N<sub>4</sub> sites was  $-0.807$  eV and  $-0.349$  eV, respectively. In addition, the charge density difference mappings in Fig. 4 display a stronger electron transfer between the oxidants ( $O_2$  and  $H_2O_2$ ) and the Fe-N<sub>4</sub> sites after the modification by the Fe cluster. According to the Bader charge analysis, in the presence of the Fe cluster, the transfer of charge from the Fe-N<sub>4</sub> sites to  $O_2$  and  $H_2O_2$  experienced an increase, specifically from 0.451 e and 0.048 e to 0.521 e and 0.094 e, respectively [47–49]. These results suggested that the Fe/Fe compounds could boost the electron transfer between the oxidants and the Fe-N<sub>x</sub> sites. Furthermore, calculated energy diagrams of the formation of ·OH and  $^1O_2$  are presented in Fig. 4e-f (\* denotes the adsorption site). The results demonstrated that the introduction of Fe/Fe compounds could lower the limiting energy barrier of ·OH and  $^1O_2$  formation from 2.16 eV and 1.27–1.19 eV and 1.25 eV, respectively.

#### 3.4.4. Overall removal mechanisms

As shown in Fig. S9, though  $H_2O_2$  was consumed during the reaction, 13.33  $\mu$ M  $H_2O_2$  was measured at 30 min in the Fe-N @ MBC alone system. This was because, besides the Fe-N<sub>x</sub> sites, the nZVI on Fe-N @ MBC could also activate  $O_2$  to produce  $H_2O_2$  by Eq. (1) [50]. In general, the metal ions leaching from metal-based catalysts also contribute to  $H_2O_2$  activation in heterogeneous catalytic systems. To make it clear, the concentration of  $Fe^{2+}$  detected after the Fe-N @ MBC/ $H_2O_2$  process (1.29 mg/L) was applied for  $Fe^{2+}/H_2O_2$  and  $Fe^{2+}$  alone processes. As Fig. S14 shows, the aqueous  $Fe^{2+}$  could activate  $H_2O_2$  effectively to degrade SMX, with SMX removal of 84.63% in 30 min (Eqs. (3–6)) [31, 44]. However, almost no SMX was removed in the  $Fe^{2+}$  alone system, indicating aqueous  $Fe^{2+}$  could not activate  $O_2$  for SMX destruction. It should be noted that the contribution of the leached  $Fe^{2+}$  should be lower than that obtained in Fig. S14 because the concentration of the leached ions gradually increased during the reaction.

In addition, the alterations of Fe-N @ MBC after the catalytic reactions with  $H_2O_2$  and  $O_2$  were assessed through XPS and SEM analyses (Fig. S15). As depicted in Fig. S15a-b, the surfaces of Fe-N @ MBC and the spherical particles (nZVI) on it exhibited a roughened texture after the reaction. This observation serves as evidence for the occurrence of the reactions between Fe, Fe compounds, Fe-N<sub>x</sub> sites,  $H_2O_2$ ,  $O_2$ , and  $H^+$  [28,51,52]. Furthermore, the changes in surface composition of Fe-N @ MBC were examined through XPS analysis. According to the Fe 2p XPS spectra (Fig. S15c-d), the proportion of Fe-O increased from 56.14% to 71.50%, while Fe-N decreased from 43.86% to 28.50%, providing further validation for the catalytic reactions triggered by Fe/Fe compounds and Fe-N<sub>x</sub> [31,53].



Based on the above analyses, the primary removal mechanisms of SMX in the Fe-N @ MBC/ $H_2O_2$  system were as follows: (1) adsorption through pore filling, hydrogen-bond interaction, surface complexation, and  $\pi$ - $\pi$  interaction; (2) SMX was directly degraded by PFRs and Fe/Fe compounds on the surface of Fe-N @ MBC through electron transfer; (3) PFRs, Fe/Fe compounds, Fe-N<sub>x</sub> on Fe-N @ MBC activated the oxidants

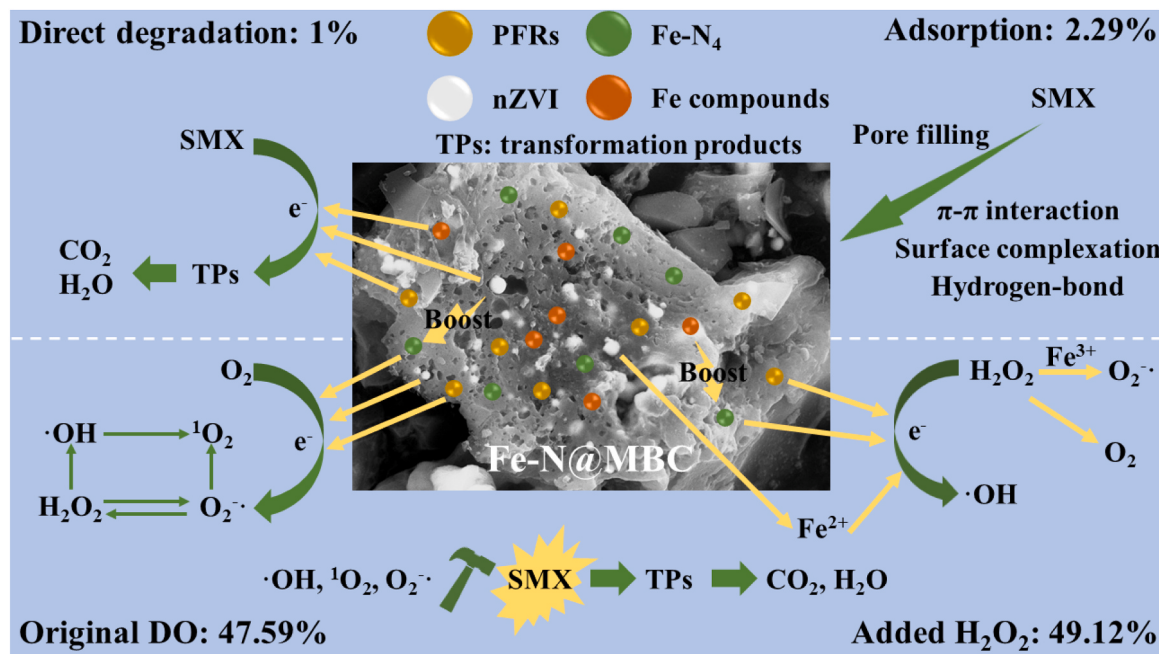


Fig. 5. Schematic diagram of SMX removal mechanisms in the Fe-N @ MBC/H<sub>2</sub>O<sub>2</sub> system. The percentages refer to the contribution of different ways to SMX removal.

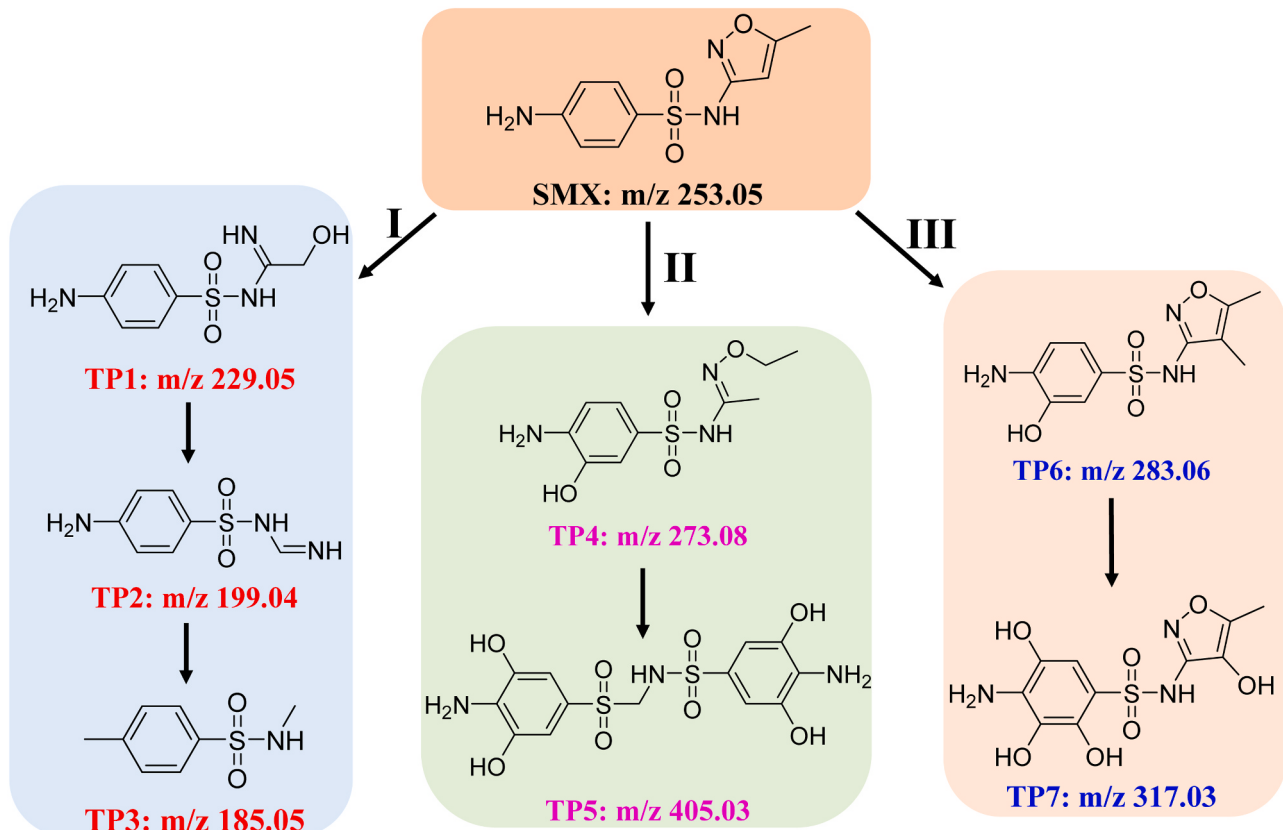
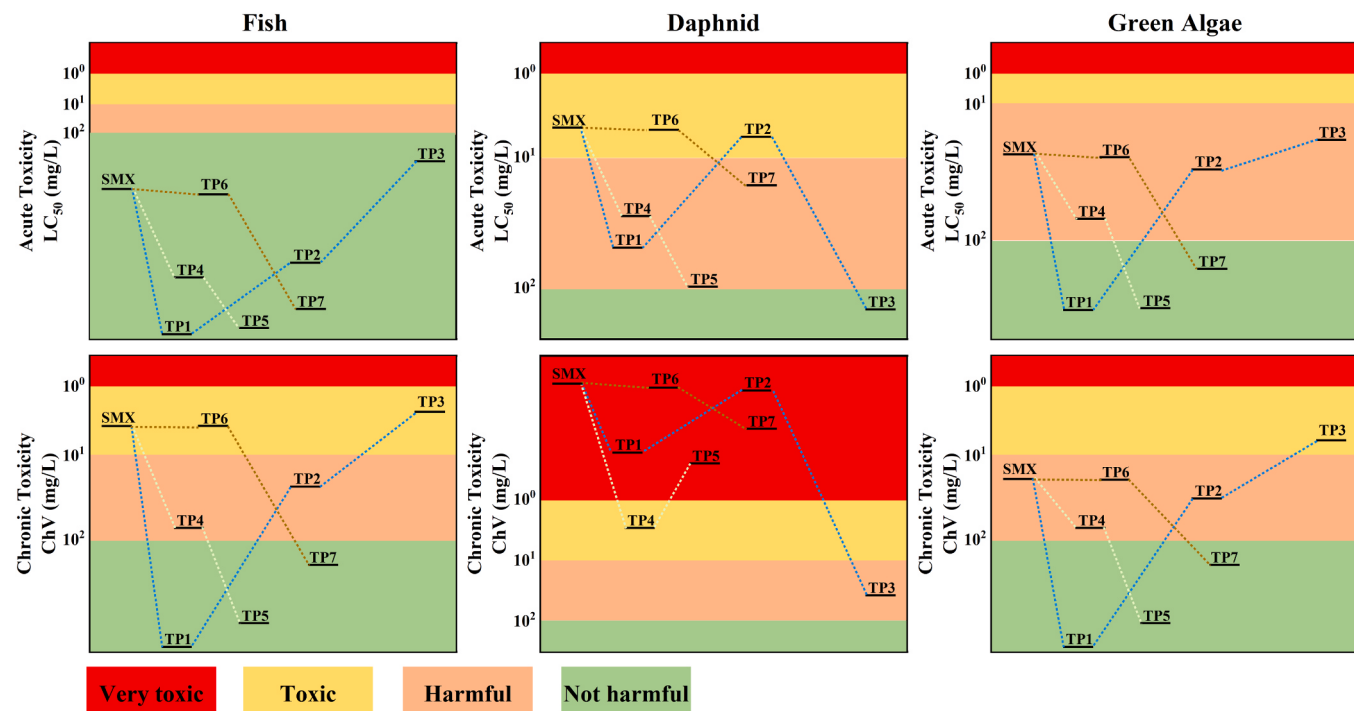


Fig. 6. Possible transformation pathways of SMX in the Fe-N @ MBC/H<sub>2</sub>O<sub>2</sub> system.

and triggered Fenton and Fenton-like reactions to produce ROS (i.e., OH, O<sub>2</sub><sup>-</sup> and <sup>1</sup>O<sub>2</sub>) for SMX degradation [41,54,55]. The details are schematically presented in Fig. 5.

### 3.5. Transformation pathways of SMX and toxicity evaluation

The Fe-N @ MBC/H<sub>2</sub>O<sub>2</sub> process resulted in the mineralization of about 16% of total organic carbon (TOC) in the solution in 30 min, indicating the transformation of SMX to other intermediates. Therefore,



**Fig. 7.** Estimated acute and chronic toxicities of SMX and its transformation products to fish, daphnid, and green algae by ECOSAR.

the transformation products (TPs) of SMX were analyzed by UPLC-MS/MS, and seven major TPs ( $m/z$  299.05, 199.04, 185.05, 273.08, 405.03, 283.06, and 317.03) were identified based on the ion fragments and proposed structures (Figs. S16-S24). Moreover, three possible transformation pathways of SMX were proposed in Fig. 6. In pathway I, SMX was degraded to TP1 by a ring-opening reaction and hydroxylation, then TP2 was obtained after the elimination of  $-\text{CH}_2\text{OH}$ , and finally, TP3 was formed by the replacement of  $-\text{NH}_2$  by  $-\text{CH}_3$  and elimination of  $=\text{NH}$ . In pathway II, TP4 was derived from the ring-opening and hydroxylation reactions of SMX, and then TP5 was obtained by the further hydroxylation and coupling reactions [27,40]. In pathway III, hydroxylation and methylation reactions occurred on SMX, resulting in the formation of TP6. Then, TP7 was formed by the further hydroxylation of TP6.

To estimate the acute and chronic toxicities of SMX and its TPs to fish, daphnid, and green algae, the ECOSAR program was employed (see Text S3 for details) [56]. As shown in Table S7 and Fig. 7, the evaluated toxicity of all TPs (except for TP3 towards fish and green algae) decreased by different degrees compared to the parent SMX. To be specific, in pathways II and III, the acute and chronic toxicities to fish and green algae reduced with the transformation. Although the acute and chronic toxicities of TP3 towards fish and green algae were slightly higher than SMX, the toxicities of TP3 to daphnid decreased significantly compared to that of the parent compound and other TPs. Therefore, the ecotoxicities of SMX would be attenuated in the Fe-N @ MBC/H<sub>2</sub>O<sub>2</sub> process.

#### 4. Conclusions

In this work, a Fe-N-C containing Fe/Fe compounds and Fe-N<sub>x</sub> coordination sites (Fe-N @ MBC) was successfully prepared using FeCl<sub>3</sub>·6 H<sub>2</sub>O and *Chlorella vulgaris* through a very simple two-step route. The  $m\text{-}k_{\text{obs}}$  of the Fe-N @ MBC/H<sub>2</sub>O<sub>2</sub> system, which stood at 124  $\mu\text{mol}\cdot\text{min}^{-1}\cdot\text{g}^{-1}$ , surpassed that of the majority of transition metal- or carbon-based activators previously reported in literature. It was further discovered that the contribution of adsorption, direct degradation, the original DO in the solution, and the added H<sub>2</sub>O<sub>2</sub> to SMX removal were 2.29%, 1%, 47.59%, and 49.12% separately. In addition,

OH, O<sub>2</sub> and <sup>1</sup>O<sub>2</sub> generated from the activation of O<sub>2</sub> and H<sub>2</sub>O<sub>2</sub> by Fe-N @ MBC were identified to be the ROS responsible for SMX destruction. Experiments and DFT calculations results suggested that the Fe/Fe compounds remarkably increased the activation performance of the Fe-N<sub>x</sub> sites by lowering the energy barrier of the ROS formation and promoting the electron transfer between Fe-N<sub>x</sub> and the oxidants. Overall, this study provides new insights into the facile synthesis, rational design, and catalytic mechanisms of Fe-N-C used in H<sub>2</sub>O<sub>2</sub>-based AOPs.

#### CRedit authorship contribution statement

**Cheng Hou:** Writing - Original Draft, Methodology, Investigation, Conceptualization. **Jiang Zhao:** Writing - review & editing, Methodology. **Libin Yang:** Methodology. **Jiabin Chen:** Writing - review & editing. **Xuefen Xia:** Funding acquisition. **Xuefei Zhou:** Funding acquisition. **Yalei Zhang:** Methodology, Funding acquisition, Supervision.

#### Declaration of Competing Interest

The authors declare that they have no known competing financial interests or personal relationships that could have appeared to influence the work reported in this paper.

#### Data availability

Data will be made available on request.

#### Acknowledgments

This work was supported by the National Key Research and Development Program of China (No. 2021YFC3200604), National Natural Science Foundation of China (U21A20322), China Baowu Low Carbon Metallurgy Innovation Foundation-BWLCF202105, and Shanghai Science and Technology Innovation Action Plan (No. 22dz1205700).

## Appendix A. Supporting information

Supplementary data associated with this article can be found in the online version at doi:10.1016/j.apcatb.2023.123135.

## References

[1] J. Skea, R. van Diemen, J. Portugal-Pereira, A.A. Khourdajie, Outlooks, explorations and normative scenarios: Approaches to global energy futures compared, *Technol. Forecast. Soc. Change* 168 (2021), 120736.

[2] Y.A. Lim, M.N. Chong, S.C. Foo, I.M.S.K. Ilankoon, Analysis of direct and indirect quantification methods of  $\text{CO}_2$  fixation via microalgae cultivation in photobioreactors: A critical review, *Renew. Sust. Energ. Rev.* 137 (2021).

[3] R. Fuller, P.J. Landrigan, K. Balakrishnan, G. Bathan, S. Bose-O'Reilly, M. Brauer, J. Caravano, T. Chiles, A. Cohen, L. Corra, M. Cropper, G. Ferraro, J. Hanna, D. Hanrahan, H. Hu, D. Hunter, G. Janata, R. Kupka, B. Lanphear, M. Lichtveld, K. Martin, A. Mustapha, E. Sanchez-Triana, K. Sandilya, L. Schaeffli, J. Shaw, J. Seddon, W. Suk, M.M. Tellez-Rojo, C. Yan, Pollution and health: a progress update, *Lancet Planet. Health* 6 (2022) e535–e547.

[4] A. Goldthau, S. Tagliapietra, Energy crisis: five questions that must be answered in 2023, *Nature* 612 (2022) 627–630.

[5] W. Wu, L. Tan, H. Chang, C. Zhang, X. Tan, Q. Liao, N. Zhong, X. Zhang, Y. Zhang, S.-H. Ho, Advancements on process regulation for microalgae-based carbon neutrality and biodiesel production, *Renew. Sust. Energ. Rev.* 171 (2023), 112969.

[6] X. You, L. Yang, X. Zhou, Y. Zhang, Sustainability and carbon neutrality trends for microalgae-based wastewater treatment: A review, *Environ. Res.* 209 (2022), 112860.

[7] Y. Chen, Global potential of algae-based photobiological hydrogen production, *Energy Environ. Sci.* (2022).

[8] C. Yang, R. Li, B. Zhang, Q. Qiu, B. Wang, H. Yang, Y. Ding, C. Wang, Pyrolysis of microalgae: A critical review, *Fuel Process. Technol.* 186 (2019) 53–72.

[9] W. Gao, Z. Lin, H. Chen, S. Yan, Y. Huang, X. Hu, S. Zhang, A review on N-doped biochar for enhanced water treatment and emerging applications, *Fuel Process. Technol.* 237 (2022).

[10] S.H. Ho, Y.D. Chen, R. Li, C. Zhang, Y. Ge, G. Cao, M. Ma, X. Duan, S. Wang, N. Q. Ren, N-doped graphitic biochars from C-phycocyanin extracted *Spirulina* residue for catalytic persulfate activation toward nonradical disinfection and organic oxidation, *Water Res.* 159 (2019) 77–86.

[11] L. Peng, X. Duan, Y. Shang, B. Gao, X. Xu, Engineered carbon supported single iron atom sites and iron clusters from Fe-rich Enteromorpha for Fenton-like reactions via nonradical pathways, *Appl. Catal. B* 287 (2021), 119963.

[12] Y. Peng, B. Lu, S. Chen, Carbon-supported single atom catalysts for electrochemical energy conversion and storage, *Adv. Mater.* 30 (2018), e1801995.

[13] J.X. Han, H.L. Bao, J.Q. Wang, L.R. Zheng, S.R. Sun, Z.L. Wang, C.W. Sun, 3D N-doped ordered mesoporous carbon supported single-atom Fe-N-C catalysts with superior performance for oxygen reduction reaction and zinc-air battery, *Appl. Catal. B* 280 (2021), 119411.

[14] Z. Ma, T. Song, Y. Yuan, Y. Yang, Synergistic catalysis on Fe-N<sub>x</sub> sites and Fe nanoparticles for efficient synthesis of quinolines and quinazolinolines via oxidative coupling of amines and aldehydes, *Chem. Sci.* 10 (2019) 10283–10289.

[15] W.J. Jiang, L. Gu, L. Li, Y. Zhang, X. Zhang, L.J. Zhang, J.Q. Wang, J.S. Hu, Z. Wei, L.J. Wan, Understanding the high activity of Fe-N-C electrocatalysts in oxygen reduction: Fe/Fe<sub>3</sub>C nanoparticles boost the activity of Fe-N<sub>x</sub>, *J. Am. Chem. Soc.* 138 (2016) 3570–3578.

[16] K. Strickland, M.W. Elise, Q.Y. Jia, U. Tylus, N. Ramaswamy, W.T. Liang, M. T. Sougrati, F. Jaouen, S. Mukerjee, Highly active oxygen reduction non-platinum group metal electrocatalyst without direct metal-nitrogen coordination, *Nat. Commun.* 6 (2015) 7343.

[17] A. Zitolo, V. Goellner, V. Armel, M.T. Sougrati, T. Mineva, L. Stievano, E. Fonda, F. Jaouen, Identification of catalytic sites for oxygen reduction in iron- and nitrogen-doped graphene materials, *Nat. Mater.* 14 (2015) 937 (–).

[18] Q. Wang, Z.Y. Zhou, Y.J. Lai, Y. You, J.G. Liu, X.L. Wu, E. Terefe, C. Chen, L. Song, M. Rauf, N. Tian, S.G. Sun, Phenylenediamine-based FeN<sub>x</sub>/C catalyst with high activity for oxygen reduction in acid medium and its active-site probing, *J. Am. Chem. Soc.* 136 (2014) 10882–10885.

[19] Y. Wang, P. Meng, Z. Yang, M. Jiang, J. Yang, H. Li, J. Zhang, B. Sun, C. Fu, Regulation of atomic Fe-spin state by crystal field and magnetic field for enhanced oxygen electrocatalysis in rechargeable zinc-air batteries, *Angew. Chem. Int. Ed.* (2023), e202304229.

[20] W. Miao, Y. Liu, D. Wang, N. Du, Z. Ye, Y. Hou, S. Mao, K. Ostrikov, The role of Fe-N<sub>x</sub> single-atom catalytic sites in peroxymonosulfate activation: Formation of surface-activated complex and non-radical pathways, *Chem. Eng. J.* 423 (2021), 130250.

[21] N. Jiang, H. Xu, L. Wang, J. Jiang, T. Zhang, Nonradical oxidation of pollutants with single-atom-Fe(III)-activated persulfate: Fe(V) being the possible intermediate oxidant, *Environ. Sci. Technol.* 54 (2020) 14057–14065.

[22] Y. Yin, L. Shi, W. Li, X. Li, H. Wu, Z. Ao, W. Tian, S. Liu, S. Wang, H. Sun, Boosting fenton-like reactions via single atom Fe catalysis, *Environ. Sci. Technol.* 53 (2019) 11391–11400.

[23] Q. Li, Y. Wang, H. Cao, S. Cui, Y. Su, A novel extraction method for analysing available sulfamethoxazole in soil, *Chem. Ecol.* 35 (2019) 284–299.

[24] T. Liu, J. Chen, N. Li, S. Xiao, C.H. Huang, L. Zhang, Y. Xu, Y. Zhang, X. Zhou, Unexpected role of nitrite in promoting transformation of sulfonamide antibiotics by peracetic acid: Reactive nitrogen species contribution and harmful disinfection byproduct formation potential, *Environ. Sci. Technol.* 56 (2022) 1300–1309.

[25] L. Jiao, G. Wan, R. Zhang, H. Zhou, S.H. Yu, H.L. Jiang, From metal-organic frameworks to single-atom Fe implanted N-doped porous carbons: Efficient oxygen reduction in both alkaline and acidic Media, *Angew. Chem. Int. Ed.* 57 (2018) 8525–8529.

[26] J.A. Rodriguez-Manzo, M. Terrones, H. Terrones, H.W. Kroto, L.T. Sun, F. Banhart, In situ nucleation of carbon nanotubes by the injection of carbon atoms into metal particles, *Nat. Nanotechnol.* 2 (2007) 307–311.

[27] Y. Xie, X. Wang, W. Tong, W. Hu, P. Li, L. Dai, Y. Wang, Y. Zhang,  $\text{Fe}_x\text{P}$ /biochar composites induced oxygen-driven Fenton-like reaction for sulfamethoxazole removal: Performance and reaction mechanism, *Chem. Eng. J.* 396 (2020), 125321.

[28] H. Lv, H. Niu, X. Zhao, Y. Cai, F. Wu, Carbon zero-valent iron materials possessing high-content fine  $\text{Fe}^{0}$  nanoparticles with enhanced microelectrolysis-Fenton-like catalytic performance for water purification, *Appl. Catal. B* 286 (2021), 119940.

[29] J. Lu, C. Zhang, J. Wu, One-pot synthesis of magnetic algal carbon/sulfidized nanoscale zerovalent iron composites for removal of bromated disinfection byproduct, *Chemosphere* 250 (2020), 126257.

[30] W. Liu, L. Zhang, X. Liu, X. Liu, X. Yang, S. Miao, W. Wang, A. Wang, T. Zhang, Discriminating catalytically active FeNx species of atomically dispersed Fe-N-C catalyst for selective oxidation of the C-H Bond, *J. Am. Chem. Soc.* 139 (2017) 10790–10798.

[31] J. Liu, K. Luo, X. Li, Q. Yang, D. Wang, Y. Wu, Z. Chen, X. Huang, Z. Pi, W. Du, Z. Guan, The biochar-supported iron-copper bimetallic composite activating oxygen system for simultaneous adsorption and degradation of tetracycline, *Chem. Eng. J.* 402 (2020), 126039.

[32] F. Xiao, W. Li, L. Fang, D. Wang, Synthesis of akageneite (beta-FeOOH)/reduced graphene oxide nanocomposites for oxidative decomposition of 2-chlorophenol by Fenton-like reaction, *J. Hazard. Mater.* 308 (2016) 11–20.

[33] X. He, Z. Liu, W. Niu, L. Yang, T. Zhou, D. Qin, Z. Niu, Q. Yuan, Effects of pyrolysis temperature on the physicochemical properties of gas and biochar obtained from pyrolysis of crop residues, *Energy* 143 (2018) 746–756.

[34] Z. Xiong, Z. Huhanwan, W. Jing, C. Wei, C. Yingguan, X. Gao, Y. Haiping, C. Hanping, Physicochemical and adsorption properties of biochar from biomass-based pyrolytic polygeneration: effects of biomass species and temperature, *Biochar* 3 (2021) 657–670.

[35] S.M. Shaheen, A. Mosa, Natasha, H. Abdelrahman, N.K. Niazi, V. Antoniadis, M. Shahid, H. Song, E.E. Kwon, J. Rinklebe, Removal of toxic elements from aqueous environments using nano zero-valent iron- and iron oxide-modified biochar: a review, *Biochar* 4 (2022) 24.

[36] Q. Huang, S. Song, Z. Chen, B. Hu, J. Chen, X. Wang, Biochar-based materials and their applications in removal of organic contaminants from wastewater: state-of-the-art review, *Biochar* 1 (2019) 45–73.

[37] J. Tang, J. Wang, Iron-copper bimetallic metal-organic frameworks for efficient Fenton-like degradation of sulfamethoxazole under mild conditions, *Chemosphere* 241 (2020), 125002.

[38] J. Yang, J.J. Pignatello, B. Pan, B. Xing, Degradation of *p*-Nitrophenol by lignin and cellulose chars:  $\text{H}_2\text{O}_2$ -mediated reaction and direct reaction with the char, *Environ. Sci. Technol.* 51 (2017) 8972–8980.

[39] G. Fang, C. Zhu, D.D. Dionysiou, J. Gao, D. Zhou, Mechanism of hydroxyl radical generation from biochar suspensions: Implications to diethyl phthalate degradation, *Bioresour. Technol.* 176 (2015) 210–217.

[40] L. Zhang, J. Chen, T. Zheng, Y. Xu, T. Liu, W. Yin, Y. Zhang, X. Zhou, Co-Mn spinel oxides trigger peracetic acid activation for ultrafast degradation of sulfonamide antibiotics: Unveiling critical role of Mn species in boosting Co activity, *Water Res.* (2022), 119462.

[41] X. Pan, Z. Gu, W. Chen, Q. Li, Preparation of biochar and biochar composites and their application in a Fenton-like process for wastewater decontamination: A review, *Sci. Total Environ.* 754 (2021), 142104.

[42] G. Fang, J. Gao, C. Liu, D.D. Dionysiou, Y. Wang, D. Zhou, Key role of persistent free radicals in hydrogen peroxide activation by biochar: implications to organic contaminant degradation, *Environ. Sci. Technol.* 48 (2014) 1902–1910.

[43] Z. Wang, A. Berbille, Y. Feng, S. Li, L. Zhu, W. Tang, Z.L. Wang, Contact-electrocatalysis for the degradation of organic pollutants using pristine dielectric powders, *Nat. Commun.* 13 (2022) 130.

[44] J. Zhao, T. Chen, C. Hou, B. Huang, J. Du, N. Liu, X. Zhou, Y. Zhang, Efficient activation of peroxymonosulfate by biochar-loaded zero-valent copper for enrofloxacin degradation: Singlet oxygen-dominated oxidation process, *Nanomaterials* 12 (2022) 2842.

[45] H. Lee, H.-i Kim, S. Weon, W. Choi, Y.S. Hwang, J. Seo, C. Lee, J.-H. Kim, Activation of persulfates by graphitized nanodiamonds for removal of organic compounds, *Environ. Sci. Technol.* 50 (2016) 10134–10142.

[46] T. Liu, S. Xiao, N. Li, J. Chen, X. Zhou, Y. Qian, C.H. Huang, Y. Zhang, Water decontamination via nonradical process by nanoconfined Fenton-like catalysts, *Nat. Commun.* 14 (2023) 2881.

[47] K. Pan, C. Yang, J. Hu, W. Yang, B. Liu, J. Yang, S. Liang, K. Xiao, H. Hou, Oxygen vacancy mediated surface charge redistribution of Cu-substituted  $\text{LaFeO}_3$  for degradation of bisphenol A by efficient decomposition of  $\text{H}_2\text{O}_2$ , *J. Hazard. Mater.* 389 (2020), 122072.

[48] Y. Song, H. Wu, Y. Liu, G. Chen, R. Jia, L. Shi, Z. Shen, G. Li, J.H. Bitter, X. Wang, L. Huang, Oxygen vacancy regulated valence states of Pt on rutile  $\text{TiO}_2$  promote catalytic oxidation of  $\text{HCHO}$ , *Appl. Catal.*, A 660 (2023).

[49] W. Ma, J. Mao, C.T. He, L. Shao, J. Liu, M. Wang, P. Yu, L. Mao, Highly selective generation of singlet oxygen from dioxygen with atomically dispersed catalysts, *Chem. Sci.* 13 (2022) 5606–5615.

[50] S.Y. Pang, J. Jiang, J. Ma, Oxidation of sulfoxides and arsenic(III) in corrosion of nanoscale zero valent iron by oxygen: Evidence against ferryl ions (Fe(IV)) as active intermediates in Fenton reaction, *Environ. Sci. Technol.* 45 (2011) 307–312.

[51] C. Hou, J. Zhao, Y. Zhang, Y. Qian, J. Chen, M. Yang, J. Du, T. Chen, B. Huang, X. Zhou, Enhanced simultaneous removal of cadmium, lead, and acetochlor in hyporheic zones with calcium peroxide coupled with zero-valent iron: Mechanisms and application, *Chem. Eng. J.* 427 (2022), 130900.

[52] G. Xue, Q. Wang, Y. Qian, P. Gao, Y. Su, Z. Liu, H. Chen, X. Li, J. Chen, Simultaneous removal of aniline, antimony and chromium by ZVI coupled with H<sub>2</sub>O<sub>2</sub>: Implication for textile wastewater treatment, *J. Hazard. Mater.* 368 (2019) 840–848.

[53] L. Zhang, J. Chen, Y. Zhang, Y. Xu, T. Zheng, X. Zhou, Highly efficient activation of peracetic acid by nano-CuO for carbamazepine degradation in wastewater: The significant role of H<sub>2</sub>O<sub>2</sub> and evidence of acetylperoxy radical contribution, *Water Res.* 216 (2022), 118322.

[54] X. Ruan, Y. Sun, W. Du, Y. Tang, Q. Liu, Z. Zhang, W. Doherty, R.L. Frost, G. Qian, D.C.W. Tsang, Formation, characteristics, and applications of environmentally persistent free radicals in biochars: A review, *Bioresour. Technol.* 281 (2019) 457–468.

[55] Y. Mei, J. Xu, Y. Zhang, B. Li, S. Fan, H. Xu, Effect of Fe-N modification on the properties of biochars and their adsorption behavior on tetracycline removal from aqueous solution, *Bioresour. Technol.* 325 (2021), 124732.

[56] N. Li, T. Liu, S. Xiao, J. Chen, Y. Xu, R. Ji, X. Zhou, Y. Zhang, Iron cycle tuned by thiosulfate in Fenton reactions: Kinetic modelling and mechanisms, *Chem. Eng. J.* 431 (2022).